

# Investigation of three-dimensional magnetization of a dolerite intrusion using airborne full tensor magnetic gradiometry (FTMG) data

M. Queitsch,<sup>1</sup> M. Schiffler,<sup>2</sup> R. Stolz,<sup>2</sup> C. Rolf,<sup>3</sup> M. Meyer<sup>4</sup> and N. Kukowski<sup>1</sup>

<sup>1</sup>*Institute of Geosciences, Friedrich-Schiller University, DE-07749, Jena, Germany. E-mail: matthias.queitsch@uni-jena.de*

<sup>2</sup>*Leibniz-Institute of Photonic Technology, DE-07702, Jena, Germany*

<sup>3</sup>*Leibniz-Institute for Applied Geophysics, DE-30655 Hannover, Germany*

<sup>4</sup>*Supracon AG, DE-07751 Jena, Germany*

Accepted 2019 February 23. Received 2019 January 22; in original form 2017 November 30

## SUMMARY

Measurements of the magnetic field are one of the most used methods in geophysical exploration. In order to reduce the degree of ambiguity of this technique during inversion and modelling, data acquired by newly available gradiometer systems based on Superconducting Quantum Interference Devices (SQUIDS) are used. These systems provide measurements of the full magnetic gradient tensor of the Earth's magnetic field, which offers a higher directional sensitivity than conventional total field magnetometers. A magnetization vector inversion (MVI) approach has been applied on data sets acquired over a dolerite intrusion in central Germany in order to model the full magnetization vector including remanent and induced components. Two different models have been created: one using only the magnetic total field anomaly (TFA) and the other based on five components of the magnetic gradient tensor. The two models show in principal the same structure, but the model based on the gradient tensor shows better defined structures. Also, magnetization amplitudes are closer to those measured on rock samples in this area. A comparison of the total magnetization vector of the rock samples and the models shows a better agreement in the vector direction of the gradient model compared to the total field model. A separation of induced and remanent contributions to the total magnetization has been performed and again shows better results when the gradient-based model is used. The effectiveness of the separation procedure will be discussed herein. The usage of gradiometer systems in an airborne geomagnetic exploration provides additional directional information, which is very helpful for MVIs. Compared to our model based on conventional TFA data, the gradient-based model features a much better agreement of the shape and magnetization of subsurface structures with those obtained from geologic<sup>-1</sup>al studies. The same, FTMG derived estimates of magnetization are more consistent with the results of measurements on rock samples.

**Key words:** Potential Field; Induced Magnetization; Remanent Magnetization; Gradient.

## 1 INTRODUCTION

Exploration and characterization of hidden magnetic structures is one of the ongoing challenges in geophysics. A very successful technique, which has been used in the past 60 yr in mineral exploration, detection of unexploded ordinance and for mapping of archaeological sites, is the measurement of local perturbations in the total magnetic field (TMI). They are caused by the shape of magnetization contrasts in the subsurface. Total magnetization is a combination of different types, that is, induced and remanent contributions ( $\mathbf{M} = \mathbf{M}_{\text{IND}} + \mathbf{M}_{\text{NRM}}$ ), which depend on the mineral

composition and conditions during formation. The induced component depends on the intensity of the magnetic background field, that is, the Earth's magnetic field  $\mathbf{F}$ , and the bulk rock susceptibility  $\chi$  ( $\mathbf{M}_{\text{IND}} = \chi\mathbf{F}$ ), whereas the remanent contribution is independent from these factors and depends mainly on the rock composition.

As a consequence of the complex magnetization, a practical problem arises for geomagnetic exploration—the ambiguity of this method, which leads to a high probability of misinterpretation. This means that, in the worst case, a planned drill campaign based on such misinterpretation can fail its desired target. As discussed by Clark (2014), various methods can be used to reduce the risk of

misinterpretation. The main idea is the modelling of the full magnetization vector (MV), including both induced and remanent contributions as well as self-demagnetization. The understanding of the interplay of these contributions may also significantly increase the value of geomagnetic data interpretation, for example, in terms of estimation of the age or rock composition. In this paper, we will focus on a geological setting with (isotropic) induced and remanent magnetizations. Anisotropy and self-demagnetization (Clark 2014) will be neglected, since both are not expected to play a significant role in the chosen study area.

Several attempts have been made to include the remanent magnetization in the modelling process using different approaches for the inverse modelling of TMI data (Kubota & Uchiyama 2005; Foss & McKenzie 2009; Lelièvre *et al.* 2009; Li *et al.* 2010; Foss & McKenzie 2011; Ellis *et al.* 2012; Pratt *et al.* 2014; Fullagar & Pears 2015; Li & Sun 2016). An often studied example is the Black Hill Norite in South Australia (Rajagopalan *et al.* 1993, 1995). For that site various approaches, including full magnetization vector inversion (MVI), have been used in order to improve the interpretation and to extract information on the remanent contribution to the total magnetization (Phillips 2005; Foss & McKenzie 2011; Macleod & Ellis 2013; Pratt *et al.* 2014). In all of these studies TMI data were used. Despite the low directional sensitivity of TMI data (Foss 2006), the direction of the remanent magnetization was successfully reproduced. It is very likely that data with improved directional information would further enhance the modelling result. This information could be provided when the full magnetic field vector  $\mathbf{B}$  would be measured instead of the TMI. However, it is difficult to achieve measurements of  $\mathbf{B}$  with high accuracy in the sub-nano-Tesla range, mostly due to overwhelming motion noise (Christensen & Dransfield 2002) and the demand of an extremely high dynamic range in the Earth's magnetic field, which is not realizable by available sensor technology and analogue-to-digital converters so far. This includes inertial measurement units (IMUs) for attitude corrections, analogue-to-digital converters and the vectorized magnetometers themselves. Measuring the spatial derivatives instead, that is, full tensor magnetic gradiometry (FTMG), using arrays of gradient sensors, the so-called gradiometers, based on Superconducting Quantum Interference Devices (SQUIDS; Schmidt *et al.* 2004; Stolz *et al.* 2006; Leslie *et al.* 2007; Rompel 2009), offers information with the desired accuracy.

In this study we aim to explore the benefits of FTMG over conventional TMI data sets on example data acquired in central Germany over a dolerite intrusion with a significant remanent magnetization. Our main goal is to investigate the advantages or draw backs of FTMG versus TMI data in MVIs of this structure. Therefore, the shape of the magnetized zone in the inversion results will be evaluated by available geological models and the magnetization itself is compared to results of palaeomagnetic analysis of orientated rock samples.

## 2 GEOLOGICAL SETTING OF THE STUDY AREA

Our study area is located in the centre of the *Thuringian Forest*, a mountain range in central Germany (inset in Fig. 1). It is characterized by units formed during a basin-and-range type extension with contemporaneous volcanism in the *Late Carboniferous* and *Early Permian (Rotliegend)*. Hence, these units are mainly volcano-sediments with plutonic intrusions (Andreas & Lützner 2009; Fig. 1a).

The units most important in the framework of this study are the *Goldlauter* and *Oberhof* formation, as well as the *Höhenberger-dolerite*:

The *Goldlauter* formation (*Lower Rotliegend*) mainly consists of conglomerates, lacustrine sand and silt stones with pelitic and pyroclastic intercalations (Andreas & Lützner 2009). They contain volcanic material originating from older units (Lützner *et al.* 2003). Other components of the conglomerates are various metamorphic rocks (schist and quartzite), flysch sediments, andesite, and rhyolite in varying portions and grain sizes (Lützner *et al.* 2003).

The *Oberhof* formation (*Lower Rotliegend*) mainly consists of rhyolites and pyroclastic material with local interbeddings of clay sediments. This material mainly originates from intrusive and effusive magmatism along WNW–ESE striking faults (Andreas 2013). Conglomerates containing mainly rhyolitic material are also present within this formation (Andreas & Lützner 2009).

The *Höhenberger-dolerite*, a mafic intrusion, nearly cuts through the entire *Thuringian Forest* in the N–S direction. There are two active quarries in this area, the *Spittergrund* and *Nesselgrund* quarries, marked by red polygons in Fig. 1(a), at which the dolerite is still mined. This material is mostly used as building material for road constructions. The intrusive body was drilled at the site ‘Schnellbach 1/62’ (Andreas & Volland 2010). From the drill cores, it is known that the intrusion dips with 30° towards the east and is expected to dip steeper at greater depth (Lützner *et al.* 2012; see also the geologic cross-section, Fig. 1b). Indications for multiple intrusion phases have been found at the *Spittergrund* quarry (Mädler 2009) and in the drilled cores (Andreas & Volland 2010). Thus, the intrusive body might show varying magnetic properties at different locations. However, the dolerite is by far the unit with the highest magnetization in this area.

## 3 METHODS

### 3.1 The magnetic gradient tensor

The magnetic gradient tensor  $\hat{\mathbf{B}}$  is a  $3 \times 3$  matrix containing the spatial derivatives of the magnetic field vector components:

$$\hat{\mathbf{B}} = \frac{\partial B_i}{\partial x_j} = \begin{pmatrix} B_{xx} & B_{xy} & B_{xz} \\ B_{xy} & B_{yy} & B_{yz} \\ B_{xz} & B_{yz} & -B_{xx} - B_{yy} \end{pmatrix}. \quad (1)$$

Five elements of the gradient tensor are sufficient to describe the complete tensor, since the magnetic field is free of divergence and thus the tensor is traceless. Additionally, only quasi-static magnetic fields are considered, which results in the symmetry of the tensor (Pedersen & Rasmussen 1990). Working with the tensor and its components provides some advantages compared to conventional TMI data sets: (1) a higher sensitivity to shallow structures, (2) suppression of (uniform) regional magnetic fields and diurnal variations, (3) sharper anomaly delineation due to stronger decay of the signal ( $1/r^4$  instead of  $1/r^3$  for TMI) and (4) directional information provided by the different tensor components (Pedersen & Rasmussen 1990; Schmidt & Clark 2006). This is especially important in exploration, as a good estimation of the magnetization and geometry allows for a better characterization of an ore bearing body.

Additional invariant quantities can be calculated from the tensor, which are characterized by better signal-to-noise ratio (Pedersen & Rasmussen 1990; Pilkington 2014). The different directional sensitivities of the single gradient tensor components allow to infer

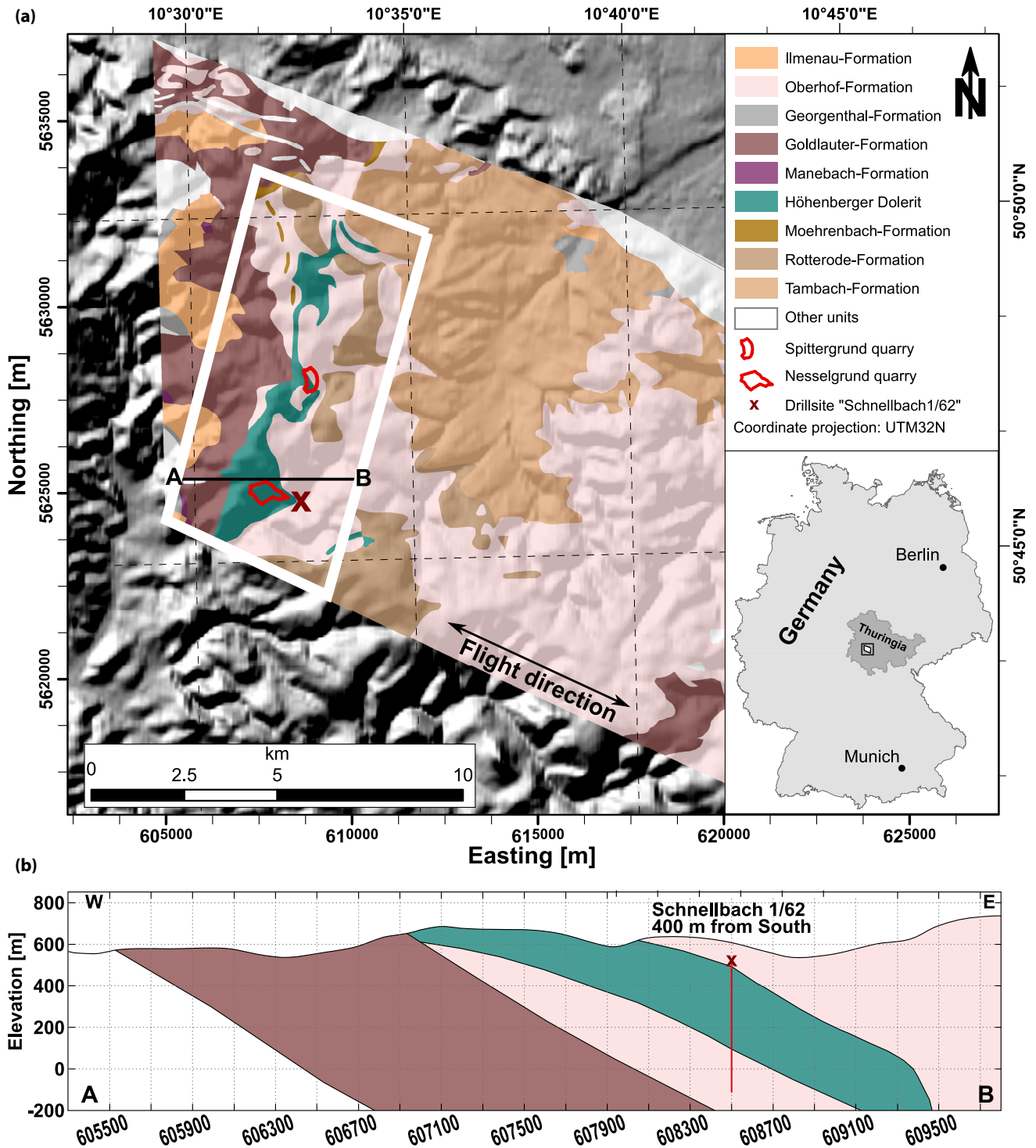


**Figure 1.** (a) Geological map of the ‘Schmalwasser’ survey area (TLUG 2003). The red polygons mark the location of the two quarries *Nesselgrund* (south) and *Spittergrund* (north). Topography is shown in the background. The white rectangle marks the location of the data subset used in this study. (b) Cross-section along the profile A–B based on the drill site ‘Schnellbach 1/62’ modified after (Andreas & Lütznier 2009).

initial information of the orientation and magnetization of the causing structure. It is also possible to calculate the elements of the gradient tensor from TMI data using Hilbert and Hilbert-like transforms (Nabighian 1984; Nelson 1988). However, this introduces possible sources of errors due to the applied fast Fourier transforms in this process. Therefore, the direct acquisition of these quantities should be preferred.

### 3.2 Airborne FTMG system

In this study, the airborne FTMG system developed at the *Leibniz-Institute of Photonic Technology* in Jena (Germany) has been deployed to acquire airborne FTMG data. This instrument uses planar-type first-order gradiometers (Stolz *et al.* 1999) based on SQUID sensors. It contains six of such gradiometers with a baseline of

3.5 cm, three orthogonal SQUID-based reference vector magnetometers, a differential GPS receiver as well as an IMU for georeferencing and attitude correction. The IMU comprises three orthogonal accelerometers and fibre optical gyroscopes.

All the magnetic sensors work inside a cooling unit at a temperature of 4.2 K, which is mounted in an aerodynamically shaped, non-magnetic and non-electrically conducting shell (Stolz *et al.* 2006; Rompel 2009; Schiffler *et al.* 2014; Queitsch 2016; Schiffler 2017). This system is towed underneath a helicopter, for example, using non-magnetic nylon ropes.

### 3.3 Processing

The processing of airborne FTMG data comprises several mandatory steps in order to achieve a high-quality data set: At first, the effects of parasitic responses in the gradiometer signals caused by the homogeneous Earth's magnetic field have to be removed (Vrba 1996), using the signals from the three orthogonal reference magnetometers.

The second step includes the decomposition of the various gradiometer signals into tensor components, since each planar-type gradiometer is arranged in a way to measure a mixture of all tensor components. This can be done by using a set of five of the six gradiometers. Only the gradiometer channels with the lowest noise level are selected to ensure high data quality. At this point, the tensor components are in the coordinate frame of the airborne system and have to be re-orientated into an Earth-centred-Earth-fixed (ECEF) coordinate system. This is achieved by using the signals of three orthogonal accelerometers, three fibre optical gyroscopes and a differential GPS receiver. From these signals, the attitude of the complete system can be expressed in *Euler* angles (Shin & El-Sheimy 2004), which allows to rotate the acquired gradiometer signals into the ECEF frame.

Additional processing includes removal of data points affected by man-made noise, for example, measurements close to power lines, settlements, active antennas or railways. Also, a tensorially consistent microlevelling is applied. This levelling procedure does not alter the consistency of the tensor, that is, the basic properties symmetry and tracelessness are untouched. This is achieved by combining the approaches of Weiszfeld (1937) and Mauring & Kihle (2006). Lastly, Hilbert transforms are used to calculate the magnetic field vector from the magnetic gradient tensor (Schiffler *et al.* 2017), allowing to generate the total field anomaly (TFA) data set in the same process.

### 3.4 3-D inversion of FTMG and TFA data

The inversion is carried out for the MV of rectilinear cells based on the method proposed by Zhdanov (2002). The main goal of this algorithm is to minimize Tikhonov's parametric functional (Tikhonov & Arsenin 1977):

$$P^\alpha = \phi_d(\mathbf{m}) + \alpha s(\mathbf{m}), \quad (2)$$

where  $\mathbf{m}$  is the model vector and  $\phi_d$  the data misfit functional or  $L_2$  norm of the difference between observed ( $\mathbf{d}_{\text{obs}}$ ) and predicted ( $\mathbf{d}_{\text{pre}}$ ) data:

$$\phi_d = \|\mathbf{d}_{\text{pre}} - \mathbf{d}_{\text{obs}}\|_2^2 = \|\hat{K}\mathbf{m} - \mathbf{d}_{\text{pre}}\|_2^2. \quad (3)$$

In eq. (2),  $s(\mathbf{m})$  is the stabilizer functional and  $\alpha$  is the regularization parameter, controlling the influence of the stabilizer  $s(\mathbf{m})$  and the

misfit functional  $\phi_d$ .  $\hat{K}$  is the sensitivity matrix. Two different stabilizer functionals were used. The *minimum-norm* ( $s_{\text{mn}}$ ) functional (Zhdanov 2002) is

$$s_{\text{mn}}(\mathbf{m}) = \int_V (\mathbf{m} - \mathbf{m}_{\text{apr}})^2 dv \quad (4)$$

and the *minimum-support* ( $s_{\text{MS}}$ ; Last & Kubik 1983; Portniaguine & Zhdanov 1999; Zhdanov 2002) functional is

$$s_{\text{MS}}(\mathbf{m}) = \int_V \frac{(\mathbf{m} - \mathbf{m}_{\text{apr}})^2}{(\mathbf{m} - \mathbf{m}_{\text{apr}})^2 + \beta^2} dv. \quad (5)$$

Throughout the inversion process the stabilizer functional is changed from a *minimum-norm* stabilizer at the beginning to a *minimum-support* stabilizer after the fifth iteration. This process has been proven to be successful in recovering the MV in previous studies and is called 'focused' inversion (Portniaguine & Zhdanov 1999; Čuma *et al.* 2012).

A dipole source in the centre of each rectilinear cell defines its magnetization. This makes the forward operator quite simple and fast (Zhdanov 2002). However, this introduces an error when the distance between the observation point and the model cell is small. For larger distances between source (model cell) and receiver (magnetometer), this error can be neglected. Smaller cells are used for the uppermost part of the model, in order to minimize this effect in areas with strong topography and varying ground clearance. At greater depths the vertical cell size is increased to reduce computation time.

## 4 DATA ACQUISITION

### 4.1 Airborne magnetic gradiometry survey

The airborne FTMG data were acquired in cooperation with the Federal Institute for Geosciences and Natural Resources of Germany during two campaigns in 2012 and 2013 by towing the airborne system on a 30 m long nylon rope underneath a helicopter. The complete survey site covers an area of 12.5 km  $\times$  18 km. A line spacing of 100 m resulted in 121 flight lines and 2200 line km. The data sampling rate was 1 kHz during the survey, which was decimated down to 10 Hz during processing. Thus, in flight direction a reading was taken approximately every 3 m, considering a survey speed of about 110 km hr<sup>-1</sup>. The survey was draped with an aimed ground clearance of 30 m. However, due to strong topographic changes and trees, the final ground clearance was ranging from 20 to 200 m (46 m mean). The complete data set was processed using the work flow outlined earlier.

For this study, we used a subset of the entire data set covering an area of 4.8 km  $\times$  10.3 km in the western part of the survey area. This subset contains five linear independent magnetic gradient tensor components ( $B_{xx}$ ,  $B_{xy}$ ,  $B_{xz}$ ,  $B_{yy}$ ,  $B_{yz}$ ) and the TFA (Fig. 2) calculated from the tensor. The two quarries *Spittergrund* and *Nesselgrund* are marked by red polygons in the maps (Figs 1 and 2).

### 4.2 Palaeomagnetic sampling and analysis

Orientated rock samples were collected in the quarries *Spittergrund* and *Nesselgrund* (white dot and asterisk in Fig. 2) near the central part of the *Höhenberger* dolerite intrusion. The natural remanent magnetization (NRM) and susceptibility of these samples were measured in order to evaluate inversion results. The sampling locations are marked in Fig. 2 by a white dot and asterisk. Rock samples were collected using two different techniques (Butler 1992): (1)

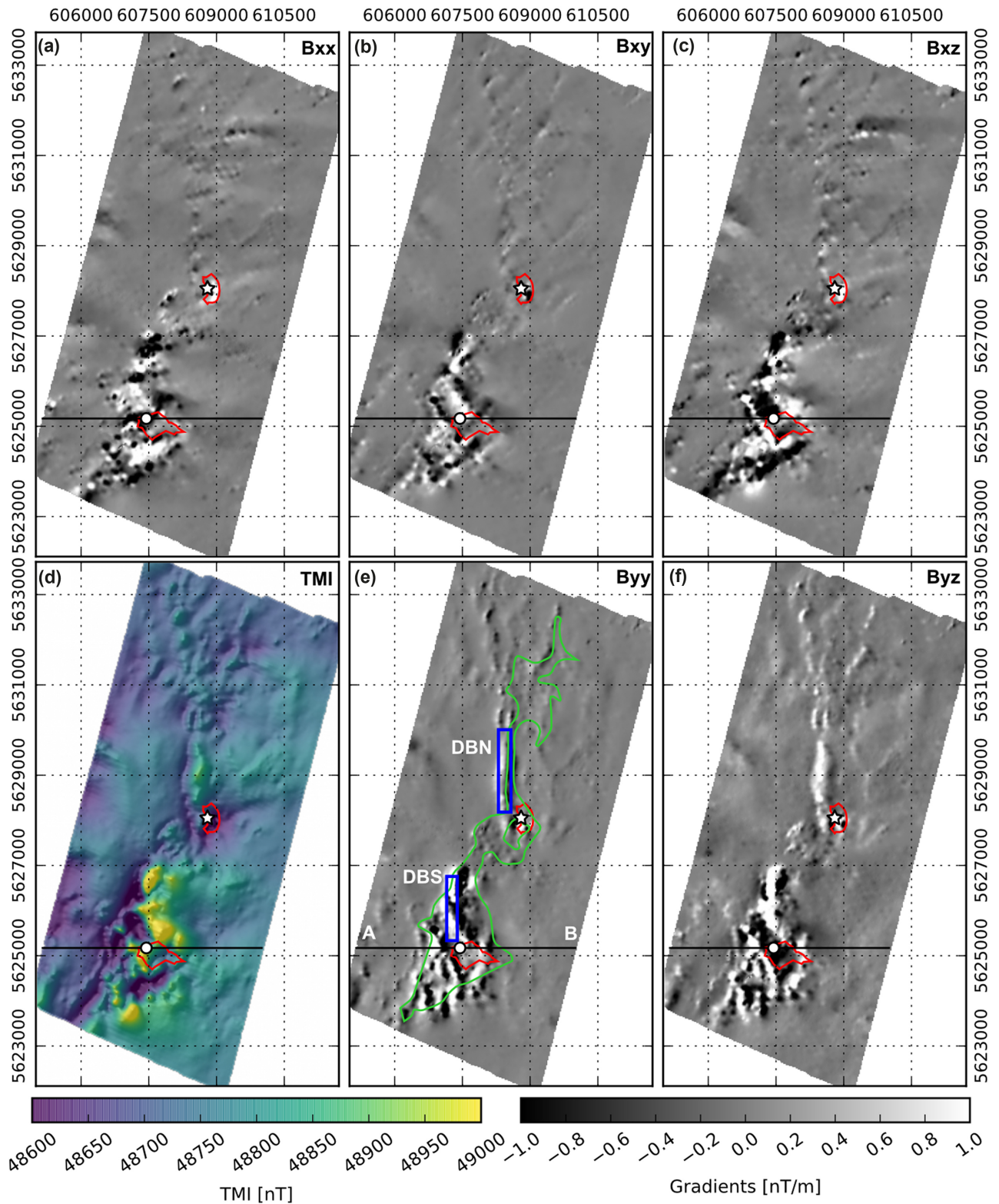


**Figure 2.** Measured magnetic tensor components  $B_{xx}$  (a),  $B_{xy}$  (b),  $B_{xz}$  (c),  $B_{yy}$  (e),  $B_{yz}$  (f) and the TMI (d) of the study area. The black line (i.e. profile A–B in Fig. 1b) marks the position of the slice through inversion result. The two sample positions are marked by the white dot and asterisk for *Spittergrund* and *Nesselgrund*, respectively. In panel (e) the outline of the dolerite intrusion as derived from the geological map and the location of the starting models used later in the inversion of the data sets are marked. The magnetization of these bodies DBN and DBS is given in Table 1. Coordinates are given in the UTM32N projection.

**Table 1.** Parameters of the two bodies used as starting models during the inversion. The locations of both structures are depicted in Fig. 2 with blue boxes.

Property	DBN	DBS
Dip angle	75°	80°
width	215 m	165 m
Top	640 m a.s.l.	710 m a.s.l.
Bottom	360 m a.s.l.	175 m a.s.l.
Magnetization $M_x$	-0.127 A m <sup>-1</sup>	-0.304 A m <sup>-1</sup>
Magnetization $M_y$	-0.399 A m <sup>-1</sup>	-1.436 A m <sup>-1</sup>
Magnetization $M_z$	0.419 A m <sup>-1</sup>	1.758 A m <sup>-1</sup>

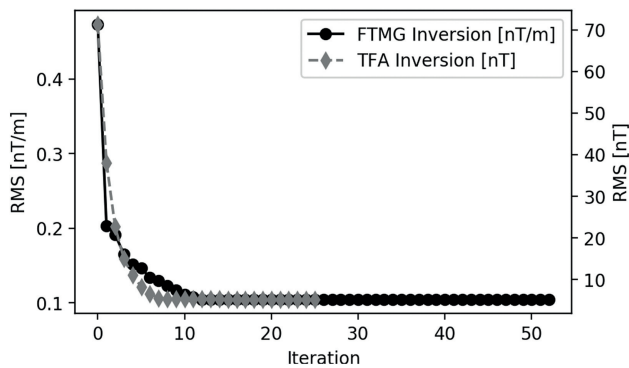


**Figure 3.** Convergence plots of the two inversion runs. The TFA inversion was terminated after the seventh iteration, while the FTMG inversion took 52 iterations.

by drilling and measuring the orientation of rock cylinders with a diameter of 2.54 cm (one inch) and a length of 5–7 cm and (2) by collecting hand samples with gypsum markers for orientation. Further analysis was performed at the magnetic laboratory of the *Leibniz-Institute for Applied Geophysics* in Grubenhagen, Germany (Rolf 2000). This included the preparation of specimens with appropriate dimensions of each sample, before measuring the magnetic susceptibility of each specimen, as well as the determination of the natural magnetic remanence.

## 5 RESULTS

### 5.1 Inversion

In order to achieve comparable results, the same discretization was applied for the FTMG and TFA inversion runs. In the model, a finer mesh was used for the uppermost 40 layers, consisting of 25 m × 25 m × 12.5 m in order to minimize possible sources of errors due to the steep topography. The lowermost cells had the same size in northern and eastern directions, but a larger vertical extension of 50 m. Both inversions had an *a priori* model consisting of two tabular dipping bodies with an eastern dip direction (DBN—dipping body north; DBS—dipping body south) and MV estimated using simple forward calculations. These bodies are shown in blue in Fig. 2 and are located at the centre of the main magnetic anomaly. Detailed parameters of these bodies are given in Table 1.

The FTMG inversion included the gradient tensor components  $B_{xz}$ ,  $B_{yz}$ ,  $B_{xy}$  and  $B_{yy}$ . This inversion run was terminated after 52 iterations because of a small relative model change. For the first five iterations, minimum-norm was used. The minimum-support stabilizer was applied after this iteration for the remaining steps. The regularization parameter  $\alpha$  (eq. 2) was determined automatically.

For the TFA inversion a fixed value for  $\alpha$  of  $3 \times 10^{-3}$  was used. It was terminated after seven iterations due to very small relative change in the model update in conjunction with low residuals. Thus, the minimum-support stabilizer was used only for two iterations. However, our test to apply this stabilizer at the third iteration did not result in lower residuals or significantly different models.

The residuals of the FTMG inversion range between 142 and 317 pT m<sup>-1</sup> (RMS) for the different gradient tensor components and 8.9 nT for the TFA inversion. An overall noise value for the measured magnetic gradient tensor components of about 50 pT m<sup>-1</sup> was estimated from the standard deviations of the inertial measurement unit channels, which means that the data has not been overfitted. To further illustrate the quality of the inversion results, we provide a convergence plot in Fig. 3 and maps with observed and predicted data (Figs 4a and b & d and e), as well as residuals in Figs 4(c) and (f). These maps prove that the main anomaly is well explained by both models. Differences are mainly caused by strong shallow anomalies with short wavelengths.

### 5.2 FTMG and TFA models

The resulting models of the MVI using the FTMG and TFA data sets are shown in Figs 5 and 6, respectively.

Both figures show horizontal and vertical slices through the final models (panels a–d), as well as the direction and amplitude of selected MVs (panels e and f) for comparison with results of the orientated rock samples. The volumes selected for the comparison are marked by rectangles in the vertical slices.

The magnetization model based on the FTMG data set shows a strong and complex magnetization pattern in the southern part of the study area (Figs 5a–c, arrow (1)), around the Nesselgrund quarry. In the north, the volume of higher magnetization is of far simpler structure and elongated in the north–south direction (arrow (2)). The down- and eastward magnetization is in general much stronger compared to the northward component. This was already expected on the base of the different gradient tensor components as shown in Fig. 2. In the northern part of the study area the location of the magnetized volume coincides very well with the outline of the mapped location of the dolerite shown in Fig. 1(h). The vertical slice in panel (d) reveals the eastward dipping nature of the structure with an angle of about 45°. The extension of the magnetized volume with depth does not entirely fit with the dolerite occurrence in the geological models. However, the map view suggests a more complex magnetization pattern in this part of the study area, and in consequence there are some discrepancies to the geological model shown in Fig. 1(b). According to the profile A–B shown in Fig. 5(d), the dolerite is exposed at the surface between 607 000 and 607 800 m easting in this coordinate projection. The magnetization model shows some smaller magnetized zones at the surface around the sampling location marked by the triangle at the surface. This part of the cross-section does not show uniform magnetic properties.

A small volume of the magnetization model was selected in order to compare its MVs with the results from measurements on orientated rock samples. The location of the box was chosen with the following criteria in mind: (1) located in the area where the dolerite is expected, (2) close to the centre<sup>-1</sup> of the highest absolute magnetization and (3) close to the sampling location at the Nesselgrund quarry. The inversion result is a total MV, which includes different types of magnetization. The directions of these vectors in the volume are given in Fig. 5(e) with the red dots. The Fisher mean directions (square; Fisher 1953) as well as the circle of 95 per cent

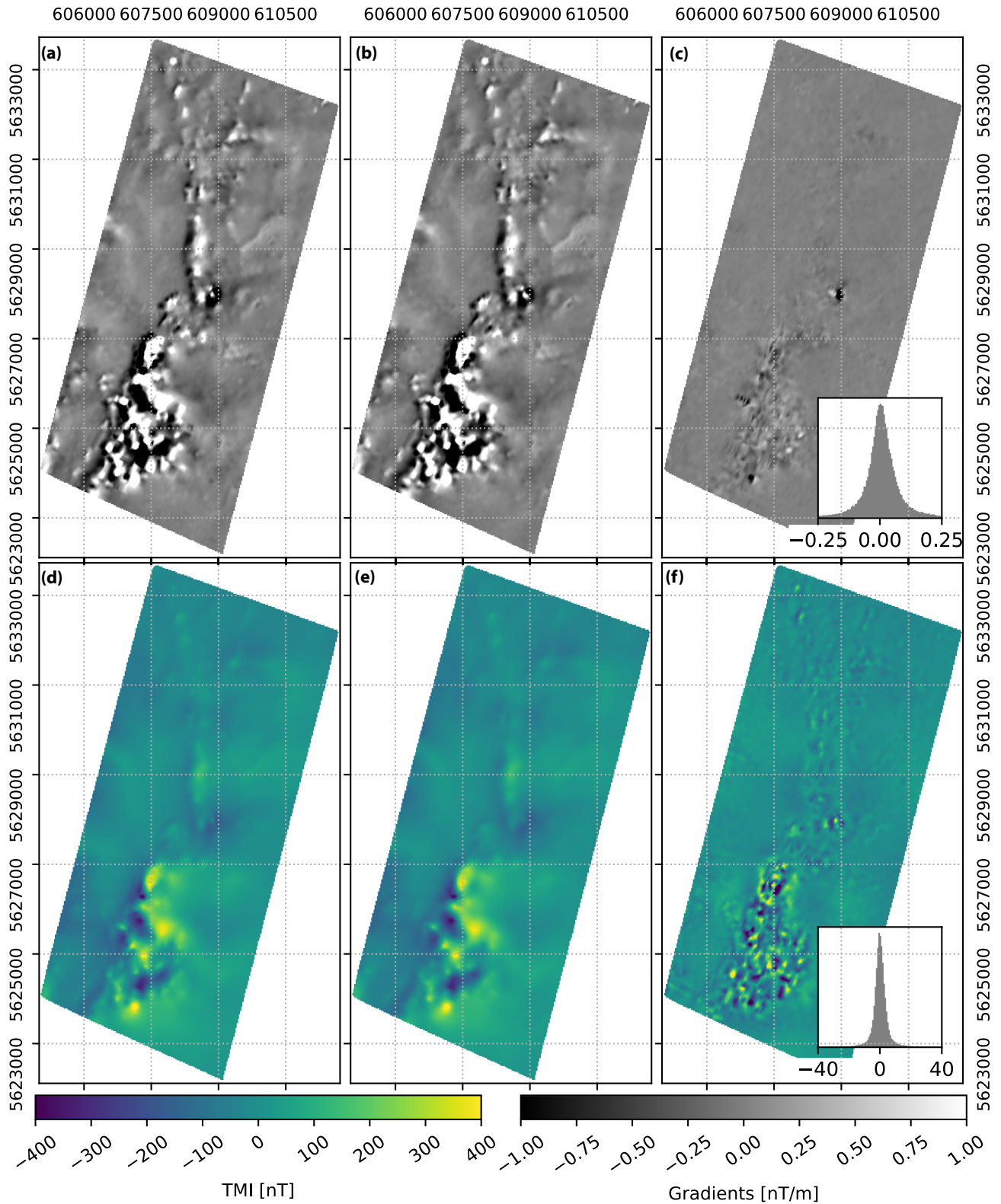


**Figure 4.** Maps showing the difference between the predicted and the observed TFA and the magnetic field gradients. The tensor component  $B_{zz}$  is given in panels (a) observed, (b) predicted and (c) residuals (observed – predicted). The TFA is given in panels (d) observed, (e) predicted and (f) residuals (observed – predicted). The colour scaling in (f) is set to  $\pm 40$  nT. Inlays in panels (c) and (f) show the histograms of the residuals. Coordinates are in the UTM32N projection.

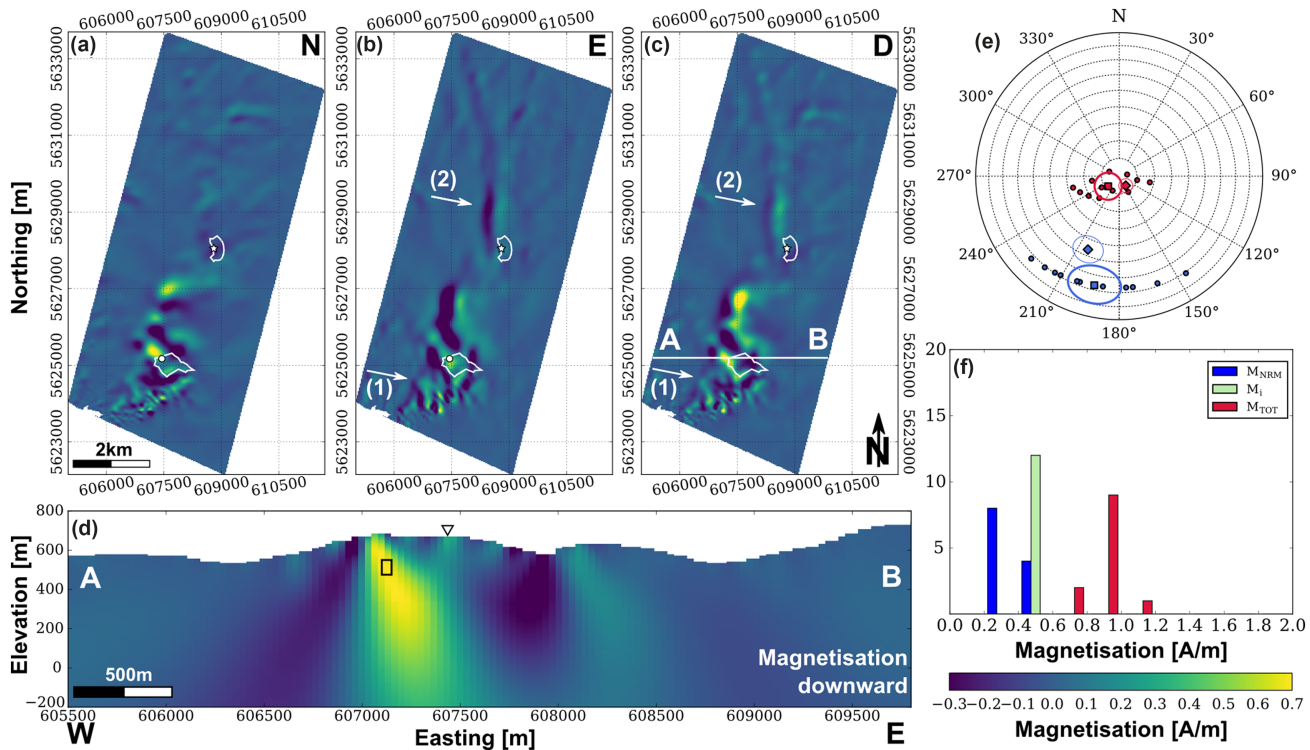


**Figure 5.** Slices through the FTMG magnetization model. Horizontal slices for the three magnetization directions in northward, eastward and downward directions at an elevation of 400 m above sea level are given in panels (a), (b) and (c). A vertical slice of the downward magnetization along an E–W-profile at the Nesselgrund quarry is shown in panel (d). In panels (e) and (f) the directions and magnetization amplitudes of a small volume (black box in panel d) of the model are depicted. The total magnetization is shown with red dots, the expected direction of the remanence is shown with blue dots. Squares denote the Fisher mean directions in the model, diamonds denote the Fisher mean of the orientated rock samples from Fig. 7. Coordinates are in the UTM32N projection.

confidence ( $\alpha_{95}$ ) are shown, too. The mean directions obtained from the orientated rock samples (see Fig. 7a) are represented by the diamonds. The Fisher mean of the inclination  $I_{\text{FTMG}}$  and declination  $D_{\text{FTMG}}$  for the total magnetization in this area of the FTMG model are  $81.6^\circ$  and  $227.6^\circ$ , respectively (Fig. 5e).

A simple separation of the induced and remanent contribution to the total MV was performed. For this separation, the assumption was made that the magnetization parallel to the Earth’s magnetic field ( $I = 66.5^\circ$  and  $D = 2.8^\circ$ ) is induced magnetization and the residuals represent remanent contribution. A result from this assumption is that the extracted remanent contribution is perpendicular to the Earth’s field direction and aligned along a great circle. Anisotropic effects cannot be derived from the total MV. Depending on the direction of the anisotropy, this contribution splits up into a parallel and a perpendicular part. Self-demagnetization however is neglected, as the overall magnetization is too low for this effect to be significant (Clark 2014). The extracted remanent contribution is shown as blue dots Fig. 5(e) with a Fisher mean of  $I = 23.2^\circ$  and  $D = 192.9^\circ$ . The amplitudes of the magnetization are lower than the measured ones by a factor of about 3.3.

TFA inversion (Fig. 6) shows very similar results in terms of the general structure and location of the magnetized material. However, the resulting TFA models are much smoother and the contacts are less well defined compared to the FTMG model. The dip of the magnetized zone depicted in panel d) has an angle of about  $40^\circ$  to  $45^\circ$ , similar to the FTMG model. Below sea level the geometry of the structure is not very well recovered in both models. Because the transitions of magnetized zones in the TFA model are much smoother, a larger volume would need to be magnetized in order to

fit the observed data. Therefore, the amplitudes of the magnetization are lower than those of in the FTMG-based model as well as at the orientated rock samples. Similar as we did with the FTMG model, the MVs in the small model volume, denoted by the rectangle (Fig. 6d), are analysed with respect to the magnetization direction of the orientated samples. The Fisher mean of the total magnetization in the TFA model has an inclination  $I_{\text{TFA}}$  and declination  $D_{\text{TFA}}$  of  $62.4^\circ$  and  $260.1^\circ$ , respectively. The estimated contribution of the remanent magnetization points towards the west with  $I = 16.7^\circ$  and  $D = 228.8^\circ$  (Fig. 6e).

### 5.3 Magnetization of rock samples

Fig. 7(a) shows the NRM directions in blue and the total magnetization in red. We calculated the mean directions, the circle of 95 per cent confidence ( $\alpha_{95}$ ), and the Fisher precision parameter ( $\kappa$ ) again using the method of Fisher (1953). The magnetization amplitudes of all specimens are also given in the histogram in Fig. 7(b). The mean directions will be used later for comparison of the directions recovered by the MVI. In order to calculate the strength of the induced magnetization, a background field with an inclination  $I = 66.5^\circ$ , declination  $D = 2.8^\circ$ , and strength  $F = 39 \text{ A m}^{-1}$  was assumed. These parameters were also used to calculate the amplitude and directions of the total magnetization.

Palaeomagnetic analysis shows a direction of the remanent magnetization with an inclination of  $I_{\text{sample-NRM}}$  of  $43.8^\circ$  and  $D_{\text{sample-NRM}}$  of  $203.1^\circ$ . In combination with the susceptibility measurements, this results in a direction for the total magnetization of  $I_{\text{sample-total}}$  of  $83.5^\circ$  and  $D_{\text{sample-total}}$  of  $145.3^\circ$ . The mean ratio between the induced

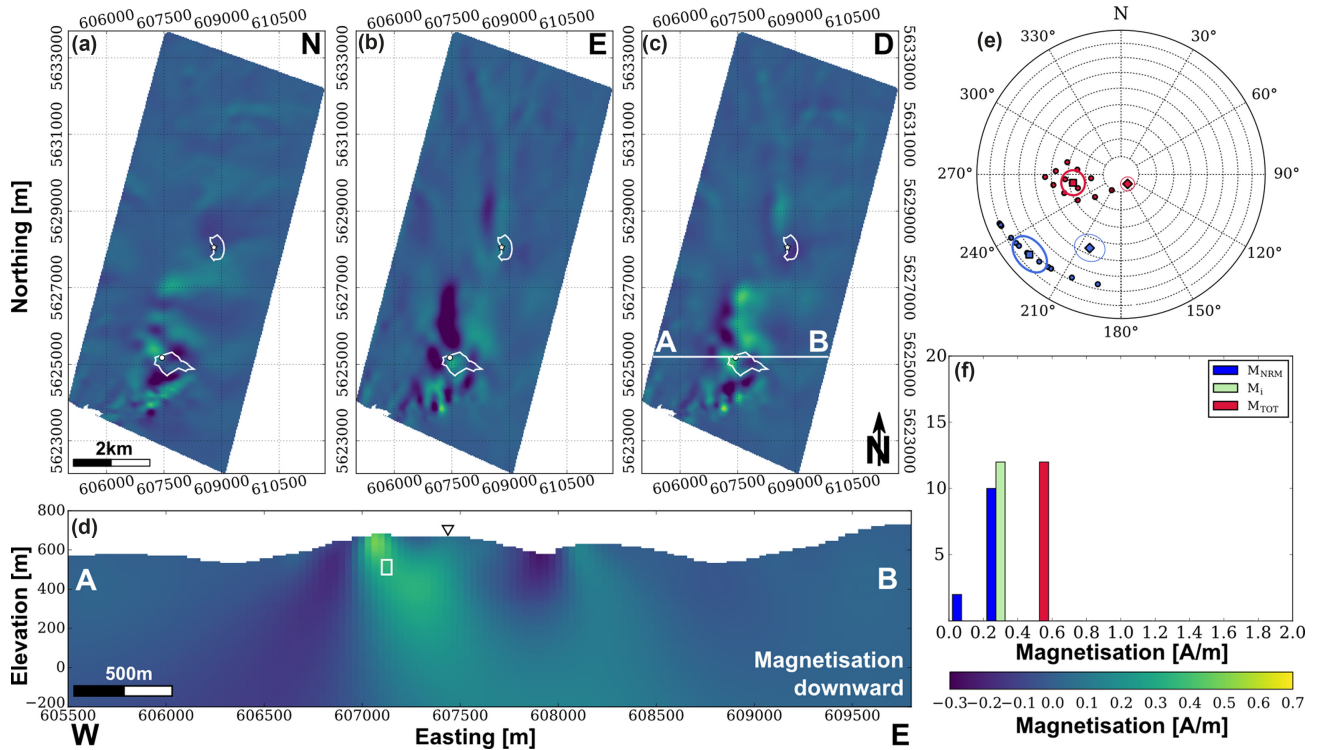


**Figure 6.** Slices through the TFA magnetization model. Again, horizontal slices at an elevation of 400 m above sea level of the three magnetization vector components in panels (a), (b) and (c). A vertical slice at the Nesselgrund profile of the downward magnetization is shown in panel (d). The direction and amplitudes of the small volume, denoted by the white rectangle in (d), are given in (e) and (f). The total magnetization is shown with red dots, the expected direction of the remanence is shown with blue dots. Squares denote the Fisher mean directions in the model, diamonds denote the Fisher mean of the orientated rock samples from Fig. 7. Coordinates are in the UTM32N projection.

and remanent magnetization  $Q$  (Koenigsberger factor) for all of the specimens is about 0.5, which means that the main contribution is caused by induced magnetization. However, the influence of the remanence is still significant and cannot be neglected. The parameters of the Fisher statistics are given in Table 2.

## 6 DISCUSSION

Inversion of potential field data sets is inherently ambiguous. In case of magnetic field data sets, not only the geometry has to be reconstructed, but also the magnetization, which is a vectorized property.

When using additional directional information provided by FTMG data, a better constrained determination of the shape of the structure and its magnetization direction should be achieved. This suggestion has been tested by carrying out two inversions using an FTMG and a TFA data set, respectively. In both cases, the differences between the observed and predicted magnetic field are quite low, and thus these models explain the data reasonably well.

### 6.1 Discussion of inversion results

Similar results were achieved in both inversions, regarding the location and shape of the structures. This includes the vertical extent, the dip direction and angle of the zones with higher magnetization. The main differences of the results is the smoothness of both models. Since the target structure is an intrusive body, sharp contacts and discontinuities of the magnetic properties are expected at its edges. Thus, compact zones of more or less uniform properties should

resemble a more reasonable model of an intrusion. The final inversion results highlight that the FTMG-based inversion shows much sharper and stronger magnetized zones. The explanation of the differences between the models can be twofold: either the increased directional sensitivity of the magnetic gradient tensor helps to better constrain the reconstruction of the structure and therefore results in sharper contacts, or it is an effect caused by the differences in the regularization and overall amount of iterations. However, in all of the inversion runs, the FTMG-based model resulted in sharper contacts, suggesting that the directional information has a significant positive impact on the results.

The inversion of the TFA data converged much faster and took only seven iterations, while the FTMG inversion was terminated after 52, mainly because the TFA inversion only had to fit one observation per datum point, whereas the FTMG inversion had to fit five components. The change in the regularization scheme from *minimum-norm* to *minimum-support* was applied at the fifth iteration, and thus the *minimum-support* stabilizer should have a greater impact on the FTMG model. However, the most significant model updates are performed within the first iterations. Depending on the damping factor  $\alpha$ , the data set can be over- or underfitted, leading to too blocky or too smooth inversion results. This unwanted behaviour is avoided by a damping factor automatically determined during the inversion (Zhdanov 2002). Therefore, an over- or underfit of the data should not have occurred during inversion. Inversion algorithms, like the one used in this study, will cause MVs to sweep over different directions at discontinuities in the model but not change abruptly as they should. This effect can be minimized by applying an appropriate regularization scheme, starting model or by using stronger constraints, that is, fixing model parameters

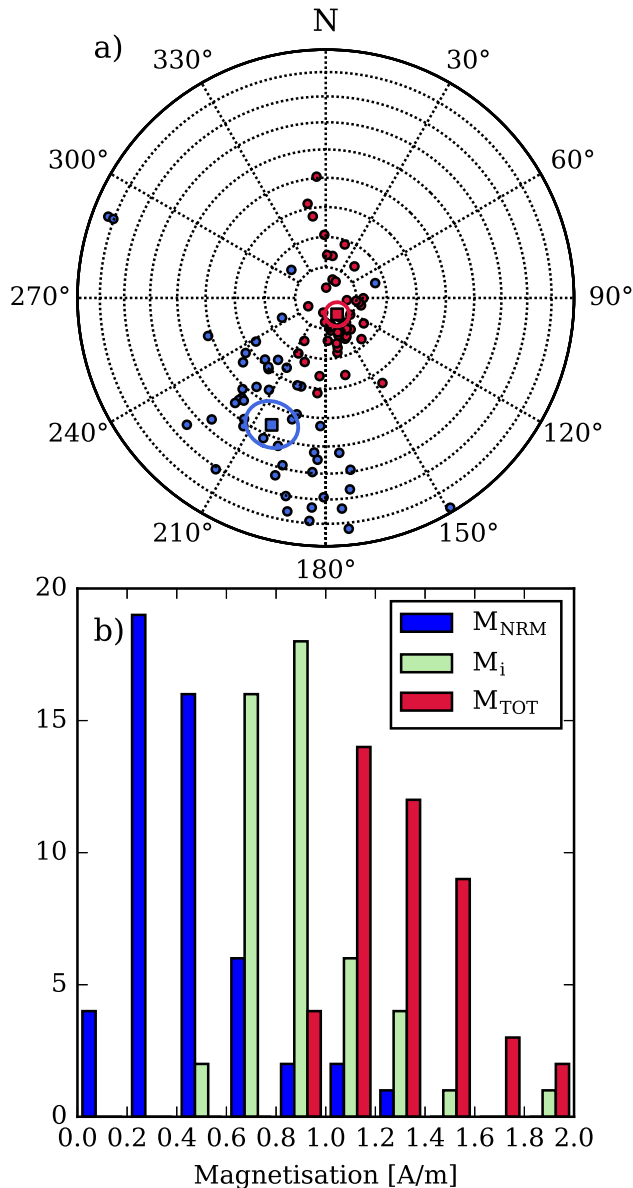


**Figure 7.** (a) Magnetization directions of all 50 samples collected in both quarries. NRM directions are shown in blue and total magnetization is in red. Squares denote the mean directions calculated using Fisher statistic (Fisher 1953) with confidence ellipses. A histogram of all magnetization amplitudes is shown in panel (b). This also includes the induced magnetization in light green calculated using the measured susceptibility values.

for certain cells. This requires a very profound knowledge of the geological structures and their petrophysical properties, for example, due to in situ measurements in boreholes and on core samples in the laboratory. Unfortunately, such data is not available in this area. The convergence plots in Fig. 3 clearly show that both inversions did converge after the 7th and 15th iteration for the TFA and FTMG inversions, respectively, and therefore can be considered as representative models. After the seventh iteration, the TFA inversion stopped automatically due to the termination criterion of 1 per cent of relative misfit. This criterion is commonly used in TFA inversions (Zhdanov 2002) and prevents models with shallow artefacts. Even though the FTMG inversion run did converge earlier, the 1 per cent criterion was not reached after 52 iterations. The final FTMG model did not show strong near surface artefacts and is

therefore considered a valid representation of the subsurface magnetization. The applied regularization scheme favours smooth and continuous models. Thus, strong anomalies with short wavelengths are difficult to reproduce using this regularization scheme, which is clearly visible in the residual maps shown in Figs 4(c) and (f).

## 6.2 Shape of the dolerite intrusion in magnetization models

The geometry of the intrusion, as suggested by the geological profile (Fig. 1b), has been confirmed with an eastward dipping body in both models. The FTMG model shows a very well defined contact and a better delineation of the structure, compared to the TFA-based model. However, the dip angle is steeper by about 15° than suggested by the geological profile.

According to this profile, the dolerite is exposed between 606 900 and 608 100 m, but both models show a much narrower extent of the zone of stronger magnetization. In addition to this discrepancy between the geological profile and the magnetization model, we do not see evidence for a uniform but rather a more complex magnetization within the dolerite. This can already be seen in the mapped magnetic gradients, but it becomes very clear in the depth slices of both models. Therefore, we suggest at least three eastward dipping tabular-like dipping bodies in the area.

Different facies were observed in the dolerite by Andreas & Voland (2010). It is therefore very likely that magnetic properties show a stronger variation as expected, which would support our suggestion of the presence of different magnetized bodies or zones in this area. A more detailed investigation of the different facies and their magnetic mineralogy would be necessary to develop a model that would satisfy the mapped geology as well as the magnetic field measurements. Such an investigation is very difficult in this area, because of the dolerite only being exposed at the two quarries. The *Nesselgrund* quarry in the south covers only a small part of the complex magnetized area and both quarries have a limited accessibility, due to an ongoing mining activity. Additionally, the collected samples already showed a strong variability in their magnetic properties, which makes the construction of a more complex model very difficult.

## 6.3 Total magnetization of FTMG versus TFA model

In order to evaluate the magnetization in the inversion results, mean directions obtained from the selected volumes are compared with the orientated rock samples. The Fisher mean of the magnetization direction obtained from the FTMG model ( $I_{\text{FTMG}} = 81.6^\circ$ ;  $D_{\text{FTMG}} = 227.6^\circ$ ) shows only a small deviation of 9.9° from the mean direction of the total magnetization of the orientated samples ( $I_{\text{Samples}} = 83.5^\circ$ ;  $D_{\text{Samples}} = 145.3^\circ$ ). For the TFA model, this deviation is 30.7° ( $I_{\text{TFA}} = 62.4^\circ$ ;  $D_{\text{TFA}} = 260.1^\circ$ ). A difference of 9.9° is very low and therefore, the magnetization in the FTMG based model can be considered to be more accurate compared to the TFA based model. It should be noted that, depending on the size and position of the selected volumes in the model, the MV will be different. This also means that the values for Fisher precision parameter  $\kappa$  and circle of 95 per cent confidence  $\alpha_{95}$  of the Fisher statistics are not reliable when characterizing directions from an MVI. Analysing the MVs in a larger volume will most likely result in lower values for  $\kappa$  and higher values for  $\alpha_{95}$ . However, the magnetization in the selected volume should be representative since it fulfils the criteria mentioned earlier.

**Table 2.** Fisher statistics (Fisher 1953) of the results of the orientated rock samples and the cells within the volume in the FTMG and TFA magnetization models.

	Incl.	Decl.	$N$	$\kappa$	$\alpha_{95}$
Samples $\mathbf{M}_{\text{tot}}$	83.5°	145.3°	50	27.2	3.9°
Samples $\mathbf{M}_{\text{NRM}}$	43.8°	203.1°	50	7.2	8.1°
FTMG $\mathbf{M}_{\text{tot}}$	81.6°	227.6°	12	32.9	7.7°
TFA $\mathbf{M}_{\text{tot}}$	62.4°	260.1°	12	41.1	6.9°

#### 6.4 Extraction and validation of remanent magnetization from magnetization models

We have also attempted to separate the induced and remanent magnetization by using a very simplifying assumption: The magnetization parallel to the Earth's field direction is treated as purely induced contribution and the residuals as remanent magnetization. This however leads to the effect that the remanence is aligned along a great circle with 90° difference around Earth's field direction. The Fisher mean of the expected remanence in the FTMG model is  $I_{\text{FTMG}} = 23.2^\circ$  and  $D_{\text{FTMG}} = 192.9^\circ$  as well as  $I_{\text{TFA}} = 16.7^\circ$  and  $D_{\text{TFA}} = 228.8^\circ$  in the TFA model. This is quite different to the measured NRM direction of the orientated rock samples (22.2° difference for the FTMG and 34.7° for the TFA model). However, when only rock samples with the highest remanence are selected ( $M \geq 0.5 \text{ A m}^{-1}$ ,  $I = 33.2^\circ$ ,  $D = 192.6^\circ$ ,  $N = 18$ ,  $\kappa = 10.2$ ,  $\alpha_{95} = 11.4^\circ$ ), the difference between the FTMG model and the rock samples is as low as 9.8°. The difference between this subset and the remanence direction extracted from the TFA based model with 38.7° is even higher. The subgroup of rock samples shows Fisher parameters with a tighter confidence circle and less scattering, which suggests that the direction of the remanent magnetization should be more reliable. This is, considering the simplicity of the separation method and the relatively unconstrained inversion, a very good agreement in the magnetization directions. Nevertheless, this method of separation is definitely not perfect and should be used with utmost caution to avoid misinterpretations. In order to improve the separation, spatial susceptibility information would be necessary. Two methods have been proposed by other authors to collect this information: (1) differential vector magnetometry (Schmidt & Clark 1997) and (2) by applying airborne frequency domain electromagnetic systems (Huang & Fraser 2001; Tschirhart *et al.* 2013). Especially the second method might have the potential to improve the MVI of FTMG data and the subsequent separation of induced and remanent magnetization contributions. However, both methods are not available to the authors and thus have not been applied in this study.

#### 6.5 Geological setting

As mentioned in the previous chapters, regarding the shape of the modelled magnetization and the mapped anomalies, there are some differences between the geological map (Andreas & Lütznier 2009) and the mapped magnetic anomalies.

Since the total magnetization is almost vertical and the dolerite is orientated in a north–south striking direction, the anomalies in the gradient tensor components  $B_{yz}$  and  $B_{yy}$  should be located almost directly above the dolerite intrusion. Therefore, differences in the location of the dolerite in the geological map and the measured magnetic anomaly may indicate areas where the magnetic data can complement future geological mapping and lead towards an improvement of the geological map.

In the south, around the *Nesselgrund* quarry, the outline of the mapped dolerite intrusion in the geological map does only match with the magnetic data in the western part. In the east, the outline encloses a wider area. In the area around the *Spittergrund* quarry, the magnetic anomaly is much weaker and becomes linear directly north of the quarry. There, the outline in the geological map is located a bit towards the east compared to the magnetic data. Furthermore, the magnetic anomaly suggests a larger east-west extension of the dolerite. In the north, where, according to the geological map, the intrusion gets much wider, we see no strong magnetic signal in the acquired data. Some other smaller linear features are visible, which correlate quite well with other geological units and have not been investigated in this study.

## 7 CONCLUSION

In conclusion, our results suggest that the application of airborne FTMG data yields significant advantages over conventional total field anomaly data sets. The FTMG data provided directional information and data with higher lateral resolution resulting in sharper transitions in the maps and allow for an initial guess of the magnetization direction of the causative bodies. Furthermore, this information improved the results of MVIs, as it has been shown in the two inversion runs, resulting in more compact structures with sharper transitions and a better agreement in the total magnetization direction. The estimation of the remanent magnetization contribution, obtained by applying assumptions regarding the induced magnetization, also provided a better agreement than the same procedure performed on the TFA-based models. More trusted results of remanence estimation may be achieved by applying robust methods that allow for a direct measurement of the magnetic susceptibility, for example, electromagnetic methods. In the future, a combination of these methods may allow for a better initial interpretation of geological structures early on in the exploration procedure, when only little information of the geological setting in the study area is available. This approach has also the potential to avoid misinterpretations and, in the worst case, drillings missing their target.

## ACKNOWLEDGEMENTS

The research presented in this study was funded by the German Federal Ministry of Education and Research (BMBF) under grant no. 03IS2091-A,C,F (INFLUINS). We thank H. Lütznier for detailed information on the geology of the dolerite intrusion. The help of U. Meyer, B. Siemon and their team of the Federal Institute for Geosciences and Natural Resources (BGR) during the airborne field campaigns and for providing the helicopter is gratefully acknowledged. We thank M. Zhdanov and the associate editor for their valuable comments, which helped to improve the manuscript.

## REFERENCES

- Andreas, D., 2013. Der Thüringer Wald im Zeitraum der Stefan-Unterperm-Entwicklung - ein Abschnitt der Zentraleuropäischen N-S-Riftzone innerhalb des Mitteleuropäischen Großschollenscharniers, *Dissertation*, Friedrich-Schiller Universität, Jena, pp. 188.
- Andreas, D. & Lütznert, H., 2009. Schichtenfolge und Paläotektonik der Rotliegend im mittleren Thüringer Wald zwischen Friedrichroda und Steinbach-Hallenberg, *Geowissenschaftliche Mitteilungen von Thüringen*, **13**, 141–161.
- Andreas, D. & Voland, B., 2010. Der Dolerit der Höhenberge - Teil eines eigenständigen Höhenberg-Intrusionsintervalls - sein Gesamtprofil in der Bohrung Schnellbach 1/62 und die Einordnung der Intrusion in den Ablauf der Rotliegendentwicklung des Thüringer Waldes, *Beitr. Geol. Thüringen*, **17**, 23–82.
- Butler, R.F., 1992. *Paleomagnetism: Magnetic Domains to Geologic Terranes*, Blackwell Scientific Publications.
- Christensen, A.N. & Dransfield, M.H., 2002. Airborne vector magnetometry over banded iron-formations, in *SEG Technical Program Expanded Abstracts 2002*, pp.13–16, doi:10.1190/1.1816921.
- Clark, D.A., 2014. Methods for determining remanent and total magnetisations of magnetic sources—a review, *Explor. Geophys.*, **45**, 271–304.
- Čuma, M., Wilson, G.A. & Zhdanov, M.S., 2012. Large-scale 3D inversion of potential field data, *Geophys. Prospect.*, **60**, 1186–1199.
- Ellis, R.G., de Wet, B. & Macleod, I.N., 2012. Inversion of magnetic data for remanent and induced sources, *ASEG Extended Abstr.*, **2012**, 1–4.
- Fisher, R., 1953. Dispersion on a sphere, *Proc. R. Soc. A*, **217**, 295–305.
- Foss, C.A., 2006. Improvements in source resolution that can be expected from inversion of magnetic field tensor data, *Leading Edge*, **25**, 81–84.
- Foss, C.A. & McKenzie, B.K., 2009. Strategies to invert a suite of magnetic field anomalies due to remanent magnetization: an example from the Georgetown area of Queensland, *ASEG Extended Abstr.*, **2009**, 1–18.
- Foss, C.A. & McKenzie, B.K., 2011. Inversion of anomalies due to remanent magnetisation: an example from the Black Hill Norite of South Australia, *Aust. J. Earth Sci.*, **58**, 391–405.
- Fullagar, P.K. & Pears, G.A., 2015. Remanent magnetisation inversion, *ASEG Extended Abstr.*, **2015**, 1–4.
- Huang, H. & Fraser, D.C., 2001. Mapping of the resistivity, susceptibility, and permittivity of the earth using a helicopter-borne electromagnetic system, *Geophysics*, **66**, 148–157.
- Kubota, R. & Uchiyama, A., 2005. Three-dimensional magnetization vector inversion of a seamount, *Earth Planets Space*, **57**, 691–699.
- Last, B.J. & Kubik, K., 1983. Compact gravity inversion, *Geophysics*, **48**, 713–721.
- Lelièvre, P.G., Oldenburg, D.W. & Williams, N.C., 2009. Integrating geological and geophysical data through advanced constrained inversions, *Explor. Geophys.*, **40**, 334–341.
- Leslie, K., Blay, K., Clark, D.A., Schmidt, P.W., Tilbrook, D., Bick, M., Foley, C. & Binks, R., 2007. Helicopter trial of magnetic tensor gradiometer, *ASEG Extended Abstr.*, **2007**, 1–4.
- Li, Y. & Sun, J., 2016. 3D magnetization inversion using fuzzy c-means clustering with application to geology differentiation, *Geophysics*, **81**, WC1–WC18.
- Li, Y., Shearer, S.E., Haney, M.M. & Dannemiller, N., 2010. Comprehensive approaches to 3D inversion of magnetic data affected by remanent magnetization, *Geophysics*, **75**, L1–L11.
- Lütznert, H., Andreas, D., Mädler, J., Michael, J., Voigt, H., Werneburg, R., Judersleben, G. & Jungwirth, J., 2003. Siles und Rotliegend, in *Geologie von Thüringen*, pp. 215–301, ed. Seidel, G., Schweizerbart.
- Lütznert, H., Andreas, D., Schneider, J., Voigt, S. & Werneburg, R., 2012. Stefan und Rotliegend im Thüringer Wald und seiner Umgebung, *Schriftenreihe der Deutschen Gesellschaft für Geowissenschaften*, 418–487.
- Macleod, I.N. & Ellis, R.G., 2013. Magnetic Vector Inversion, a simple approach to the challenge of varying direction of rock magnetization: a forum on the application of remanent magnetisation and self-demagnetisation estimation to mineral exploration, in *23rd ASEG Conference and Exhibition*, Melbourne.
- Mädler, J., 2009. Der Lagergang des basischen bis intermediären Höhenberg-Gesteins im Thüringer Wald – ein geologisch-petrographischer Überblick, *Geowissenschaftliche Mitteilungen von Thüringen*, **13**, 69–98.
- Mauring, E. & Kihle, O., 2006. Leveling aerogeophysical data using a moving differential median filter, *Geophysics*, **71**, L5–L11.
- Nabighian, M.N., 1984. Toward a three-dimensional automatic interpretation of potential field data via generalized Hilbert transforms: fundamental relations, *Geophysics*, **49**, 780–786.
- Nelson, J.B., 1988. Calculation of the magnetic gradient tensor from total field gradient measurements and its application to geophysical interpretation, *Geophysics*, **53**, 957–966.
- Pedersen, L.B. & Rasmussen, T.M., 1990. The gradient tensor of potential field anomalies: some implications on data collection and data processing of maps, *Geophysics*, **55**, 1558–1566.
- Phillips, J.D., 2005. Can we estimate total magnetization directions from aeromagnetic data using Helbig's integrals? *Earth Planets Space*, **57**, 681–689.
- Pilkington, M., 2014. Evaluating the utility of gravity gradient tensor components, *Geophysics*, **79**, G1–G14.
- Portniaguine, O. & Zhdanov, M.S., 1999. Focusing geophysical inversion images, *Geophysics*, **64**, 874–887.
- Pratt, D.A., McKenzie, K.B. & White, T.S., 2014. Remote remanence estimation (RRE), *Explor. Geophys.*, **45**, 314–323.
- Queitsch, M., 2016. Modeling and inversion of airborne full tensor magnetic gradiometry data in the Thuringian basin and forest, *Dissertation*, Friedrich-Schiller Universität, Jena, pp. 159.
- Rajagopalan, S., Schmidt, P.W. & Clark, D.A., 1993. Rock magnetism and geophysical interpretation of the Black Hill Norite, South Australia, *Explor. Geophys.*, **24**, 209–212.
- Rajagopalan, S., Clark, D.A. & Schmidt, P.W., 1995. Magnetic mineralogy of the Black Hill Norite and its aeromagnetic and palaeomagnetic implications, *Explor. Geophys.*, **26**, 215–220.
- Rolf, C., 2000. Das Kryogenmagnetometer im Magnetiklabor Grubenhagen, in *Angewandte Geophysik - neue Geräte und ihre Anwendungen*, Geologisches Jahrbuch Reihe E, Geophysik, Vol. 52, pp. 161–188, ed. Schulz, R., Schweizerbart.
- Rompel, A. K.K., 2009. Geological Applications for FTMG, in *11th SAGA Biennial Technical Meeting and Exhibition*, Swaziland, pp. 39–42.
- Schiffler, M., 2017. Enhancements in Processing, Analysis and Inversion of Full Tensor Magnetic Gradiometry Data, *Dissertation*, Friedrich-Schiller Universität, Jena, pp. 239.
- Schiffler, M., Queitsch, M., Stolz, R., Chwala, A., Krech, W., Meyer, H.-G. & Kukowski, N., 2014. Calibration of SQUID vector magnetometers in full tensor gradiometry systems, *Geophys. J. Int.*, **198**, 954–964.
- Schiffler, M., Queitsch, M., Stolz, R., Meyer, H.-G. & Kukowski, N., 2017. Application of Hilbert-like transforms for enhanced processing of full tensor magnetic gradient data, *Geophys. Prospect.*, **65**, 68–81.
- Schmidt, P.W. & Clark, D.A., 1997. Field trialling next generation magnetics, CSIRO Exploration and Mining Report 391R, p. 64.
- Schmidt, P.W. & Clark, D.A., 2006. The magnetic gradient tensor: its properties and uses in source characterization, *Leading Edge*, **25**, 75–78.
- Schmidt, P.W., Clark, D.A., Leslie, K., Bick, M., Tilbrook, D. & Foley, C., 2004. GETMAG - a SQUID magnetic tensor gradiometer for mineral and oil exploration, *Explor. Geophys.*, **35**, 297–305.
- Shin, E.H. & El-Sheimy, N., 2004. Aided Inertial Navigation System (AINS<sup>TM</sup>) toolbox for MatLab<sup>®</sup> Software, INS/GPS Integration Software, Mobile Multi-Sensors Systems (MMSS) Research Group, the University of Calgary. Available at: <http://mms.geomatics.ucalgary.ca/Research/research.htm>.
- Stolz, R., Fritsch, L. & Meyer, H.-G., 1999. LTS SQUID sensor with a new configuration, *Supercond. Sci. Technol.*, **12**, 806–808.
- Stolz, R., Zakosarenko, V., Schulz, M., Chwala, A., Fritsch, L., Meyer, H.-G. & Köstlin, E.O., 2006. Magnetic full-tensor SQUID gradiometer system for geophysical applications, *Leading Edge*, **25**, 178–180.
- Tikhonov, A.N. & Arsenin, V.I.A., 1977. *Solutions of Ill-posed Problems*, Scripta Series in Mathematics, Winston.
- TLUG(Thuringian Geological Survey), 2003. *Geological Map of Thuringia 1:200.000*.

- Tschirhart, P., Morris, B. & Hodges, G., 2013. A new regional/residual separation for magnetic data sets using susceptibility from frequency-domain electromagnetic data, *Geophysics*, **78**, B351–B359.
- Vrba, J., 1996. SQUID gradiometers in real environments in *SQUID Sensors: Fundamentals, Fabrication and Applications*, pp. 117–178, ed. Weinstock, H., Springer.
- Weiszfeld, E., 1937. Sur le point pour lequel la somme des distances de  $n$  points donnés est minimum, *Tôhoku Math. J.*, **43**, 355–386.
- Zhdanov, M.S., 2002. *Geophysical Inverse Theory and Regularization Problems*, Vol. 36 of *Methods in Geochemistry and Geophysics*, Elsevier Science.